PHYSICAL REVIEW B **102**, 075435 (2020)

Exchange splitting and exchange-induced nonreciprocal photonic behavior of graphene in CrI_3-graphene van der Waals heterostructures

Alexander M. Holmes,[1,*] Samaneh Pakniyat,[1,†] S. Ali Hassani Gangaraj,[2,‡] Francesco Monticone,[2,§]
Michael Weinert,[3,‖] and George W. Hanson[1,¶]
[1]*Department of Electrical Engineering, University of Wisconsin-Milwaukee, 3200 N. Cramer St., Milwaukee, Wisconsin 53211, USA*
[2]*School of Electrical and Computer Engineering, Cornell University, Ithaca, New York 14853, USA*
[3]*Department of Physics, University of Wisconsin-Milwaukee, Milwaukee, Wisconsin, 53211, USA*

(Received 26 May 2020; accepted 6 August 2020; published 20 August 2020)

The exchange splitting and resulting electromagnetic response of graphene in a monolayer chromium triiodide (CrI_3)–graphene van der Waals heterostructure are considered using a combination of density-functional theory and electromagnetic calculations. Although the effective exchange fields are in the hundreds of Tesla, for the equilibrium separation nonreciprocal effects are found to be weak compared to those for a comparable external magnetic bias. For nonequilibrium separations, nonreciprocal effects can be substantial.

DOI: 10.1103/PhysRevB.102.075435

I. INTRODUCTION

Graphite consists of parallel atomic layers of carbon atoms, the layers being weakly bound together by van der Waals (vdW) forces. As such, graphite is easily cleaved to form few layer materials, or even monolayers (graphene). Since its experimental isolation in 2004 [1], graphene has been an object of considerable study for both scientific and industrial investigators. Graphene's most notable feature is its atomic hexagonal lattice, which results in linear electronic dispersion and the presence of Dirac points at the Fermi level. As a result, electrons behave as massless particles in the vicinity of the Dirac point, leading to extraordinary electrical and mechanical properties [2].

Bulk chromium triiodide, CrI_3, also is a layered vdW material that can be easily cleaved, and is relatively stable in ambient conditions [3]. Bulk CrI_3 is a ferromagnetic (FM) insulator with a relatively high Curie temperature of $T_c =$ 61 K [3]. The two-dimensional (2D)/monolayer form of CrI_3 consists of Cr^{3+} ions and I^- ions that form edge-sharing octahedra arranged in a hexagonal honeycomb lattice with an approximate thickness of 0.6 nm. Like its bulk form, monolayer CrI_3 is also a FM insulator, with an out-of-plane easy axis and somewhat reduced T_c of 45 K [4].

The controlled growth/deposition of 2D materials can lead to vdW heterostructures that result in exceedingly thin structures with enhanced functionality. Here, we exploit the proximity exchange between a 2D ferromagnet and graphene. In its monolayer form, CrI_3 exhibits massive local Cr magnetic moments of $3\mu_B$, which potentially can induce large exchange splittings in adjacent layers of a heterostructure. Since 2D CrI_3 has a hexagonal structure, it is well lattice-matched with graphene. Magnetic order in CrI_3 has been studied experimentally in [4–8], and in other 2D magnets, such as $MnSe_2$ [9,10] and $CrGeTe_3$ [11,12]. In all cases, these 2D magnets have out of the plane magnetization. In some cases, magnetic effects can be controlled via electrostatic gating [7,8], or strain [13,14].

Enormous pseudomagnetic fields (on the order of hundreds of Tesla) and associated pseudo-Landau levels (LLs) have been predicted in strained systems [15]. Such fields do not break time-reversal (TR) symmetry, and cannot lead to nonreciprocal behavior. Importantly, the exchanged-induced fields described here do break TR: The effective Hamiltonians for both an external magnetic field and a ferro-/antiferromagnetic system contain terms that explicitly couple to the spin that are not invariant under time reversal; in contrast, the pseudomagnetic fields in strained graphene couple to charge only, and hence preserve time-reversal symmetry. Exchange interactions in similar vdW heterostructures have been considered, e.g., $Cr_2Ge_2Te_6$-graphene [16], where equilibrium exchange splittings were calculated to be approximately 5 meV, and EuS-graphene [17]. A Chern insulating state can be realized in graphene in proximity to CrI_3, via the magnetic exchange field and Rashba spin-orbit coupling [14,18]. However, to achieve this, the heterostructure needs to be compressed from its equilibrium state which increases the effective field [18].

In this work, we use first-principles density functional theory (DFT) calculations to show that the proximity exchange in graphene due to monolayer CrI_3 can result in an enormous exchange field, and then we investigate the conductivity of graphene due to the CrI_3 exchange field, and the behavior of bulk and nonreciprocal edge surface-plasmon polaritons (SPPs). A comparison is made with the conductivity and SPP properties of graphene in an external magnetic field, and significant differences are found in the two cases. We also examine Faraday rotation (FR) of graphene [19,20]. In Ref. [21] the graphene CrI_3 interface is also investigated using

---

[*] holmesam@uwm.edu
[†] pakniyat@uwm.edu
[‡] ali.gangaraj@gmail.com
[§] francesco.monticone@cornell.edu
[‖] weinert@uwm.edu
[¶] george@uwm.edu

DFT, and in Ref. [22] surface polaritons on graphene coupled to a bulk antiferromagnetic insulator were considered.

The principal findings of this work are (1) the equilibrium (minimum energy) separation between the $\mathrm{CrI_3}$ and graphene is approximately 3.75 Å, at which point the exchange splitting is 21 meV, corresponding to an effective exchange field of 100 T and a chemical potential of $\mu = -0.3\,\mathrm{eV}$, which self-biases the graphene. Referring to graphene's conductivity in the $\mathrm{CrI_3}$-graphene heterostructure, (2) LLs, which are the most prominent feature of the graphene conductivity in a strong external field, are absent in the case of the exchange field. (3) In the far-infrared considered here, the intraband conductivity is dominant, with diagonal element values that are approximately the same as isolated graphene with no applied magnetic bias and $\mu = -0.3\,\mathrm{eV}$, whereas the off-diagonal elements are similar in magnitude to those in the external bias case. (4) Because of the large diagonal conductivity response compared to having an external bias (in which case most of the Drude weight is transferred to the Landau levels), the resulting nonreciprocity due to the exchange field is considerably less then for an external magnetic field of the same strength. For smaller separation (achievable through, e.g., strain), nonreciprocal effects in Faraday rotation are still rather modest, but a unidirectional edge SPP can be found.

The article is organized as follows. In Sec. II the density functional calculations are presented, and results for exchange splittings and the corresponding effective exchange fields are given. In Sec. III the exchange-field-induced graphene conductivity is discussed, and compared with that arising from an external bias, and bulk and edge surface plasmons are considered. The edge SPPs for the exchange field are slightly nonreciprocal for the equilibrium separation, whereas for the external bias case they are highly nonreciprocal (unidirectional), tightly confined, long-lasting, and robust to material discontinuities. In Sec. IV, FR is shown for both the exchange and external bias fields, where, again, the exchange field is shown to produce modest FR. The Supplemental Material [23] contains further results from the DFT calculations, and the derivation of the edge plasmon dispersion. In the following, the suppressed time dependence is $e^{-i\omega t}$.

II. DENSITY FUNCTIONAL CALCULATIONS

Density functional calculations for graphene on $\mathrm{CrI_3}$ have been reported previously, [14], with an emphasis on the topological aspects of the compressed system. Here the focus is on the effect of the induced exchange field on the graphene electronic structure, and the implications for the calculation of optical properties discussed later; detailed first-principles calculations of the optical properties of the $\mathrm{CrI_3}$ itself have also been reported previously [29].

To model the composite system, we consider 5×5 graphene on a free-standing $\sqrt{3} \times \sqrt{3}$ $\mathrm{CrI_3}$ monolayer, Fig. 1(a), which has a small lattice mismatch of ~1%. (Additional calculations for $\sqrt{31} \times \sqrt{31}$ graphene on $2 \times 2\mathrm{CrI_3}$ are done to address the dependence on the relative twist of the layers and are discussed in the Supplemental Material [23].)

Because graphene and $\mathrm{CrI_3}$ are both layered van der Waals materials, the results presented below are only very weakly dependent on the horizontal registry between the two, as verified by considering two different less symmetric registries. The supercell Brillouin zone, which is a factor of 25 (3) times smaller than that of graphene ($\mathrm{CrI_3}$), is shown in Fig. 1(b). The interlayer separation is varied between 2.5 and 4.5 Å.

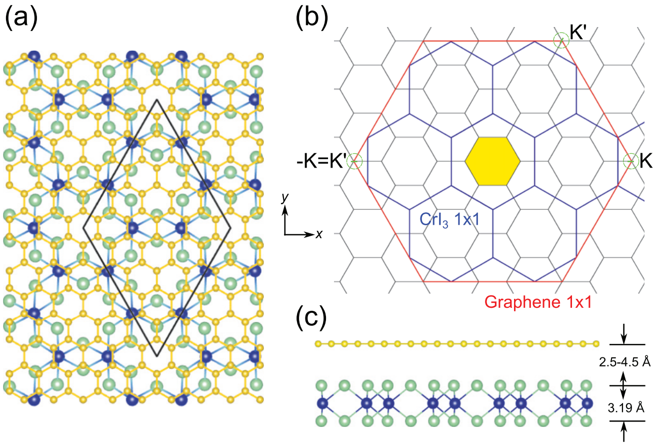

FIG. 1. (a) Top and (c) side views of the $(\sqrt{3} \times \sqrt{3})$ $\mathrm{CrI_3}$–(5×5) graphene structure (C: yellow; Cr: blue; I: green), with the commensurate supercell given in black. (b) The Brillouin zones of the supercell (black; first Brillouin zone in yellow), (1×1) $\mathrm{CrI_3}$ (blue), and (1×1) graphene (red). The green circles (and enclosed lines) denote the portion of k space where the graphene Dirac points occur.

The calculations were performed using the Vienna Ab initio Simulation Package [30] within the generalized gradient approximation (GGA)+U rotationally invariant approximation [31], with the choice of $U = 1\,\mathrm{eV}$, J=0. (As shown in Ref. [29], the $\mathrm{CrI_3}$ gap decreases with increasing U, contrary to normal expectations. This choice of parameters provides a reasonable starting point for the $\mathrm{CrI_3}$ electronic structure.) In addition, van der Waals DFT-D3 corrections [32] were included. The projector-augmented wave functions were expanded in plane waves up to 400 eV, the repeated slab geometry included a vacuum region of at least 20 Å, and a $27 \times 27 \times 1$ k-point mesh in the supercell was used for self-consistency, corresponding to a $135 \times 135 \times 1$ mesh for graphene; this mesh was sufficient for placing the Fermi level and for the optical conductivity calculations. Spin-orbit was included for some calculations (see Supplemental Material [23]) using the same parameters.

Each ferromagnetically coupled Cr has a magnetic moment of $3\,\mu_\mathrm{B}$, and the moments are calculated (~0.4 meV/Cr) to be orientated perpendicular to the plane. The spin-polarized k-projected [33,34] bands of graphene around the K point and of $\mathrm{CrI_3}$ at the calculated equilibrium graphene-$\mathrm{CrI_3}$ separation of 3.75 Å are shown in Figs. 2(a) and 2(b), respectively. (The range of separations discussed here may be experimentally accessible: the calculated pressures are 1.4, 3.7, and 13.5 GPa for separations of 3.25, 3.0, and 2.5 Å, respectively.)

The top of the $\mathrm{CrI_3}$ valence band and the lowest set of conduction bands are of majority spin (blue curves). The graphene Dirac point lies above the Fermi level in the conduction band of $\mathrm{CrI_3}$, and opens up a gap in the $\mathrm{CrI_3}$ bands along Γ-M [red circle in Fig. 2(b)]. The relative position of the graphene and $\mathrm{CrI_3}$ bands varies with interlayer separation

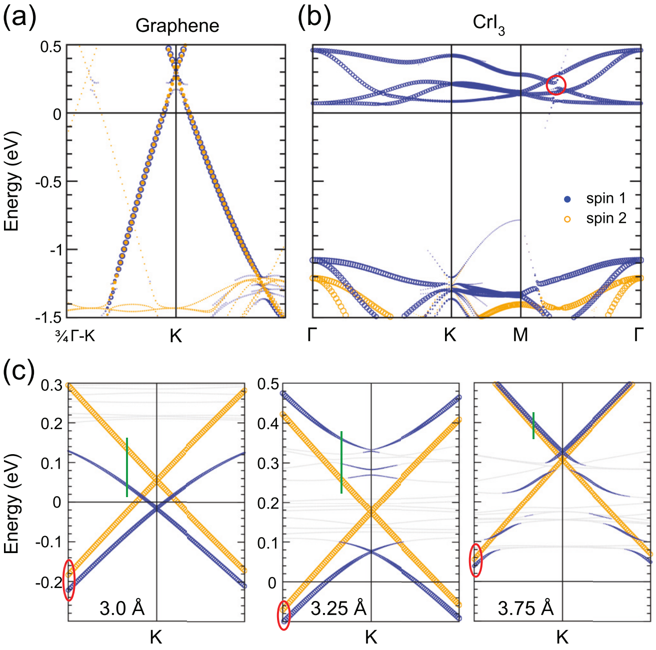

FIG. 2. *k*-projected bands of the graphene–CrI$_3$ magnetic system. Blue (orange) denote the majority (minority) spin of the CrI$_3$, and the size of the circles represents the relative weight. (a) Graphene *k*-projected bands around the K point ($\pm\frac{1}{4}$) along Γ-K of the (1 × 1) Brillouin zone, and (b) CrI$_3$ *k*-projected bands along the high symmetry directions of the (1 × 1) structure, both for a graphene–CrI$_3$ separation of 3.75 Å. (c) Close-ups of the graphene *k*-projected bands bands within $\pm\frac{1}{40}$ of K for different separations. The gray bands are ("folded" and CrI$_3$) bands with small weights. The green lines and red ovals show where the exchange splittings above and below the Dirac point, respectively, are measured.

(Fig. 2(c) and Supplemental Material Fig. S2 [23]): for separations of less than ∼3.2 Å, the graphene Dirac point is in the gap and then crosses into the CrI$_3$ conduction band. This behavior can be understood by noting that the calculated work functions and CrI$_3$ gap place the graphene Dirac point within the CrI$_3$ conduction band, for both the present GGA+U calculations and for hybrid Heyd–Scuseria–Ernzerhof functional calculations [14]. However, GW calculations for CrI$_3$ [29] increase the size of the gap, so that at the equilibrium separation the Dirac point may still be within the gap. Regardless, the present results can provide insight into the difference in expected behavior with the relative placement of the two sets of bands.

For all separations, Fig. 2(c), the minority ("spin 2") graphene bands maintain their linear dispersions, even including spin-orbit interaction (c.f., Figs. S3 and S4). The majority bands, on the other hand, interact and hybridize with the (majority spin) conduction band states even for smaller separations where the Dirac point is in the CrI$_3$ gap. Importantly, because of the proximity of the graphene to the ferromagnetic CrI$_3$, there are induced exchange splittings of the graphene bands. For larger separations, the majority graphene bands that overlap the GrI$_3$ conduction bands are strongly modified, whereas the minority bands retain the characteristic graphene dispersions.

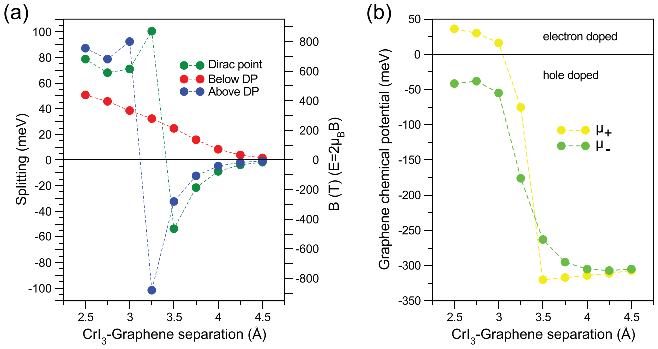

FIG. 3. (a) Exchange splittings (meV) and effective field (T), of the graphene states around K for different separations determined at the positions shown in Fig. 2(c) [above and below the Dirac point indicates the green line and red ovals, respectively, in Fig. 2(c)]. (b) The chemical potentials of graphene for each spin relative to the respective Dirac points.

The calculated splittings of the Dirac point and the bands above (below) measured at the indicated positions are given in Fig. 3(a). These splittings are large compared to the Zeeman splittings induced by an external field: the effective fields are in the range of 100 T. When the Dirac point is in the gap, the exchange splittings are normal in the sense that the majority states are deeper in energy than the minority. However, the exchange splitting of the Dirac point and the bands above reverse as the Fermi level of the combined system moves into the CrI$_3$ conduction band.

Because of the exchange splitting and the relative positions of the bands, the graphene is effectively doped, which can be described by spin-dependent chemical potentials, $\mu_\pm$, as shown in Fig. 3. For smaller separations with the Dirac points in the gap, $\mu_\pm$ are approximately equal and of opposite sign, i.e., no net doping. For larger separations, including the equilibrium one, the graphene becomes hole doped with $\mu_\pm \sim 0.3$ eV. The result is that for smaller separations when the Fermi level is in the gap, the position of the (minority) Dirac cone is closer to the Fermi level and determined by the size of the exchange splitting, while for larger separations doping determines the position; that the chemical potentials are approximately equal and much larger than the exchange splittings is physically related to the fact that local magnetic moments formation in graphene sheets is not favorable.

For graphene in external magnetic fields and nonzero chemical potential, the intraband contributions to σ_{xx} dominate over interband ones in the far-infrared optical conductivity, and the formation of Landau levels provide an explanation of the Hall conductivity σ_{xy}. Although the *effective* fields due to the proximity-induced exchange splittings are large, these do not create LLs; the formations of the minibands in the majority bands seen in Fig. 2(c) are due to interactions and hybridization with the CrI$_3$. The LLs formed in graphene in the presence of external magnetic fields or strain-induced pseudomagnetic fields [35] are both more localized in energy and have their broad momentum distribution peaked around K. Similar to LLs, however, these minibands change the dispersion and hence will modify the optical transitions.

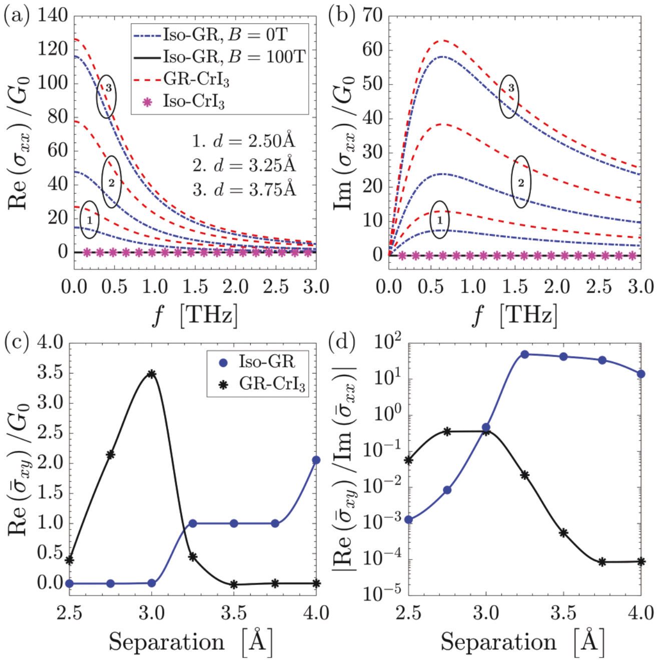

FIG. 4. (a), (b) Two-dimensional conductivity of graphene in the presence of the CrI$_3$ exchange field for separations $d \in \{2.5\,\text{Å}, 3.25\,\text{Å}, 3.75\,\text{Å}\}$. Also shown for comparison is the conductivity of isolated graphene (Iso-GR) computed assuming an external field of 100 T with chemical potential $\mu = -0.3$ eV [36], and the zero external field case using the spin dependent chemical potentials that correspond to each of the afformentioned separations (in both of the latter computations, $\Gamma = 2 \times 10^{12}$ s^{-1} and $T = 40$ K). (c) Off–diagonal element vs CrI$_3$-graphene separation compared with the isolated-graphene external bias case [where for each separation the value of effective field below the Dirac point from Fig. 3(a) was assumed. (d) The off-diagonal element normalized by the frequency average of the diagonal element. In (c), (d), the overbar indicates frequency average, as explained in the text. $G_0 = 2e^2/h$.

III. GRAPHENE CONDUCTIVITY AND SURFACE AND EDGE PLASMON POLARITONS DUE TO CrI$_3$ EXCHANGE FIELD

The computation of the intra- and interband contributions to graphene's conductivity in the presence of the CrI$_3$ exchange field is briefly described in the Supplemental Material [23]. Figure 4 shows the computed conductivity in the far-infrared and, for comparison, the conductivity computed (i) assuming isolated graphene in an external bias of 100 T and $\mu = -0.3$eV [36], the effective equilibrium exchange field and potential as described above; (ii) isolated graphene $B = 0$ T using $\mu^{\pm}$ plotted in Fig. 3(b) for separations $d \in \{2.5\,\text{Å}, 3.25\,\text{Å}, 3.75\,\text{Å}\}$; and (iii) the calculated CrI$_3$ conductivity [29], which is negligible at the considered frequencies. Figures 4(a) and 4(b) show the diagonal elements vs frequency, and Fig. 4(c) shows the off-diagonal element vs CrI$_3$-graphene separation (which are nondispersive in our calculation). For the external bias case, Fig. 4(c), the effective fields ("below the DP" values) for each "separation" from Fig. 3 were assumed. In Figs. 4(c) and 4(d), we show the mean conductivity for 0 to 5 THz. As an example, for the CrI$_3$-graphene data (for a separation of 3.75 Å), this mean is 33 G_0, and for isolated biased graphene ($B_0 = 100$ T), 0.03488 G_0.

The diagonal elements of the conductivity are dominated by the Drude intraband contribution at the considered frequencies ($\sigma_{xx}^{\text{2D}-\text{Drude}} = i\Omega/(\omega + 2i\Gamma)$, with the Drude weights Ω shown in Fig. S6), and resemble very closely the conductivity for isolated graphene with no magnetic bias, but with the exchange-field induced spin-dependent values of chemical potential $\mu^{\pm}$. Because of transfer of the Drude weight to the Landau levels in the case of an external bias, the exchange field diagonal conductivity is several orders of magnitude larger than the equivalent external field conductivity, i.e., for the external bias case, the formation of Landau levels depresses the diagonal conductivity away from the Landau level, while forcing the off-diagonal elements to be nonzero due to cyclotron motion of the charge carriers. This results in relatively large ratios of the off-diagonal to diagonal elements for the external bias, in contrast to the exchange bias case where the diagonal elements are relatively unaffected and hence the ratios are smaller.

For some separations (c.f., Fig. 3) the chemical potential is quite different for the two spins, as is the effective bias field. Therefore, for the external bias computation, we adjust the spins accordingly and sum over the two spins. For the off-diagonal elements, the exchange field values are similar in magnitude to the external bias case having the same effective field. Figure 4(d) shows the off-diagonal values of the conductivity normalized by the frequency average of the diagonal element since this ratio is an indication of the nonreciprocity of the material. Notably, the nonreciprocity of the exchange field case is much weaker than for the external field bias.

From Fig. 4, the CrI$_3$ conductivity is much smaller in magnitude than that of graphene. Since these effectively combine in parallel from an electromagnetic standpoint, we can ignore the presence of the CrI$_3$ in the electromagnetic calculations. This was confirmed by computing the dispersion of the CrI$_3$-graphene system including both conductivities, as in Ref. [37].

A. Bulk (Surface) SPPs

For the case of graphene having an arbitrary conductivity tensor and residing in a homogeneous medium characterized by μ_0 and ε, SPPs of an infinite 2D sheet satisfy a dispersion equation of the form $D(k_x, k_y) = 0$ [38], where

$$\begin{aligned} D(k_x, k_y) &= k_x k_y(\sigma_{yx} + \sigma_{xy}) + \left(k_y^2 - k_1^2\right)\sigma_{yy} + \left(k_x^2 - k_1^2\right)\sigma_{xx} \\ &\quad - 2ip\varepsilon\omega\left(1 + \tfrac{1}{4}\eta^2(\sigma_{xx}\sigma_{yy} - \sigma_{xy}\sigma_{yx})\right), \end{aligned} \tag{1}$$

$p = \sqrt{k^2 - k_1^2}$, $k = |\mathbf{k}|$ is the in-plane wave number, and $k_1 = \omega\sqrt{\mu_0\varepsilon}$. The square root in p leads to a two-sheeted Riemann surface in the q plane, and associated branch cuts. The standard hyperbolic branch cuts [39] separate the proper (where Re$(p) > 0$, such that the radiation condition as $|z| \to \infty$ is satisfied) and improper sheets.

In the presence of the exchange field, or an external magnetostatic bias, the conductivity tensor elements are

$$\begin{aligned} \sigma_{xx} &= \quad \sigma_{yy} = \sigma_d, \\ \sigma_{xy} &= -\sigma_{yx} = \sigma_o. \end{aligned} \tag{2}$$

In this case, Eq. (1) reduces to

$$D(k) = \left(p^2 - k_1^2\right)s_d - ipk_1\left(1 + s_d^2 + s_o^2\right), \tag{3}$$

where $s_d = \eta\sigma_d/2,\ s_o = \eta\sigma_o/2$, and $\eta = \sqrt{\mu_0/\varepsilon}$, and $D(k) = 0$ can be solved to yield

$$k^{\pm} = k_1\left[\frac{1}{2^2 s_d^2}\left(-is^2 \pm \sqrt{4s_d^2 - s^4}\right)^2 + 1\right]^{1/2}, \tag{4}$$

where $s^2 = s_d^2 + s_o^2 + 1$. For $s_o = 0$, Eq. (4) becomes

$$k^{+} = k^{TM} = k_1\sqrt{1 - \frac{1}{s_d^2}}, \quad k^{-} = k^{TE} = k_1\sqrt{1 - s_d^2}, \tag{5}$$

for the transverse-magnetic (TM) and transverse-electric (TE) cases, respectively, where transverse is defined with respect to the radial coordinate. For isolated and unbiased graphene characterized by isotropic complex surface conductivity, $\sigma = \sigma' + i\sigma''$, a proper TE surface wave exists if and only if $\sigma'' < 0$, and a proper TM surface wave exists for $\sigma'' > 0$. If $\mu \neq 0$, pure TM and TE modes do not exist in the presence of a magnetic bias, although usually the modes retain similar characteristics (quasi-TM/TE).

B. Edge Surface Plasmon Polaritons

Assuming an out-of-plane magnetic bias and symmetry, bulk SPPs have reciprocal dispersion; breaking symmetry, for example, by introducing an interface, allows for plasmons with asymmetrical dispersion [40]. Specifically, here we introduce a graphene half-space, and consider the quasistatic modes that may propagate on the edge. This is a well-studied problem [41,42], and here we consider the exchange field case and, for comparison, the external bias case. Two different methods of analysis are presented in the Supplemental Material [23], and a new approximate solution for SPP edge dispersion is given there [Eq. (56)].

Figure 5 shows the bulk and edge dispersions for a graphene half-space due to the exchange fields corresponding to separations of 3.0 Å, Fig. 5(a), and 3.75 Å, Fig. 5(b). For 3-Å separation, the right-going edge mode exists until approximately 3 THz, above which the edge mode leaks into the bulk SPP (mathematically, it crosses onto an improper Riemann sheet through a branch point associated with the bulk mode wave number); the leaky mode (not shown) then approximately follows the bulk dispersion, with slightly lower wave number. In this case, the edge mode is strongly nonreciprocal (unidirectional). However, for the equilibrium separation of 3.75 Å separation, the edge mode is essentially reciprocal.

The bulk and edge dispersions for graphene in an external magnetic bias field are shown in Fig. 6. The edge modes flip directions upon reversing the bias field. Although the results were computed assuming $B = 100\,\text{T}$, due to the normalization, the dispersion diagrams are essentially independent of B for $|B| \gtrapprox 1$ T. For the external bias case, the Landau levels are given by

$$M_n = \sqrt{2nv_F^2|eB|\hbar} \approx 36.3\ \text{meV}\ \sqrt{n|B|}, \tag{6}$$

where $v_F \simeq 10^6$ m/s is the graphene electron Fermi velocity.

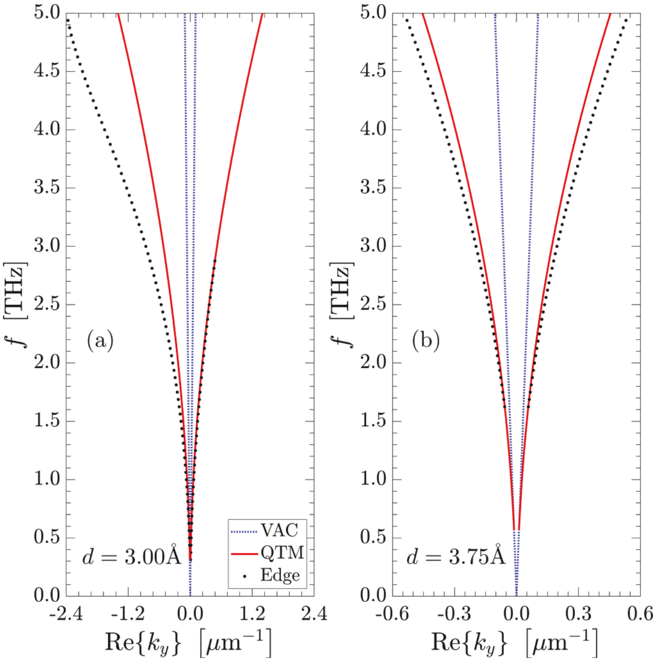

FIG. 5. Bulk (solid red) and edge (dots) TM-like dispersion of graphene modes in an exchange field for two CrI$_3$-graphene separations. VAC indicates vacuum dispersion.

For the exchange field (Fig. 5), the bulk SPPs are not gapped, whereas for the external bias case (Fig. 6) the bulk SPPs are strongly gapped. This is a result of the behavior of Im(σ): Since TM and quasi-TM modes require Im(σ) > 0 for a proper surface wave, gaps appear for Im(σ) < 0, which does not occur for the exchange case in the far-infrared, where the conductivity dispersion is Drude-like. In the external bias case, the formation of LLs causes this sign change at lower frequencies, resulting in the TM gap shown in Fig. 6.

Figures 7(a) and (7b) show edge SPP propagation length and guided wavelength on the graphene layer as a function of CrI$_3$-graphene separation. The SPP propagation length $1/2\,\text{Im}(k_y)$ generally increases with separation, and decreases with increasing frequency. The SPP wavelength is quite long, $L_{\text{SPP}}/\lambda_{\text{SPP}} \ll 1$, and so the SPP seems not to be very useful.

The corresponding edge SPP propagation length and wavelength on the graphene layer in an external field as a function of the external bias are shown in Figs. 7(c) and 7(d). As the magnetic bias increases, the SPP propagation length increases, and $L_{\text{SPP}}/\lambda_{\text{SPP}} > 1$; for large magnetic bias, $L_{\text{SPP}}/\lambda_{\text{SPP}} \approx 6-8$. For $\mu = -0.3$ eV, the results are the same as shown in Fig. 7 for $B > 80$ T, since for larger chemical potentials the SPP is not well-formed and is not quasi-TM below a critical bias [43].

Figure 8 shows the edge SPP on the exchange-field biased graphene due to a dipole source in the vicinity of the graphene-vacuum edge, computed using COMSOL. In correspondence with the dispersion shown in Fig. 5, for the equilibrium separation of 3.75 Å the SPP is essentially reciprocal, as it is at 2.5 THz for separation 3 Å. However, for 3 Å and 4 THz, the SPP is unidirectional. However, because $L_{\text{SPP}}/\lambda_{\text{SPP}}$ is short, the SPP does not propagate well.

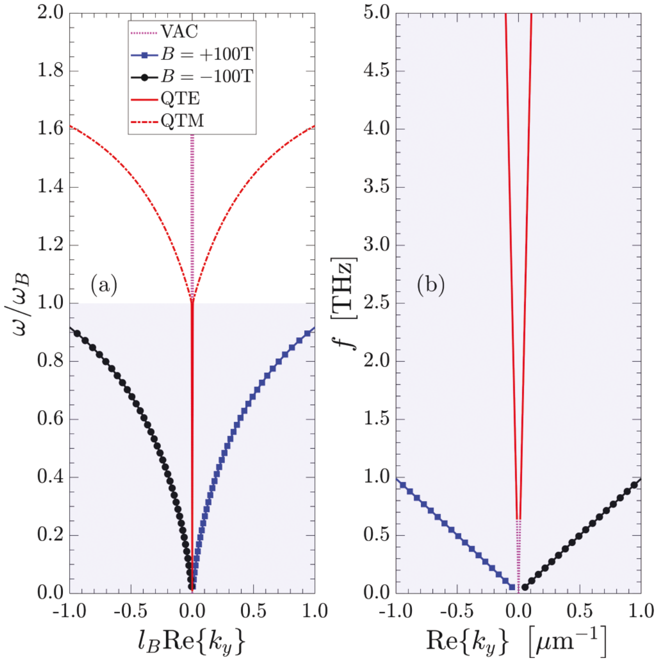

FIG. 6. Bulk (dashed red) and edge (dots) TM-like dispersion and bulk TE-like modes (solid red) for graphene in an external bias. The shaded region indicates the bulk band gap, $\omega_B = 526.2 \times 10^{12}$ is the frequency of the first Landau level, $\mu = -0.3$ eV, $T = 40$ K, $\Gamma = 2 \times 10^{12}$ s^{-1}, $B = 100$ T, and $l_B = \sqrt{\hbar/eB} = 2.6$ nm is the magnetic length.

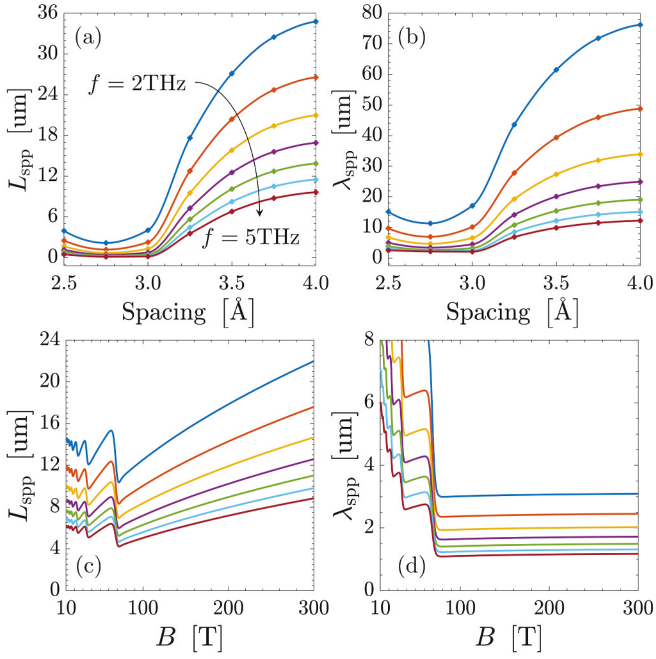

FIG. 7. (a) Edge SPP propagation length (left branch of Fig. 5) and (b) SPP wavelength on graphene in an exchange field as CrI$_3$-graphene separation varies. (c) Edge SPP propagation length and (d) SPP wavelength on graphene in an external bias for different frequencies. $\mu = 0.05$ eV, $T = 40$ K, $\Gamma = 2 \times 10^{12}$ s^{-1}. For (c) and (d), the first LL occurs at $8.8\sqrt{|B|}$, well beyond the considered frequencies. For comparison, from Fig. 3, for the separations 2.5, 3, 3.5, and 4 Å, the effective bias fields are 750, 600, 450, and 90 T, respectively.

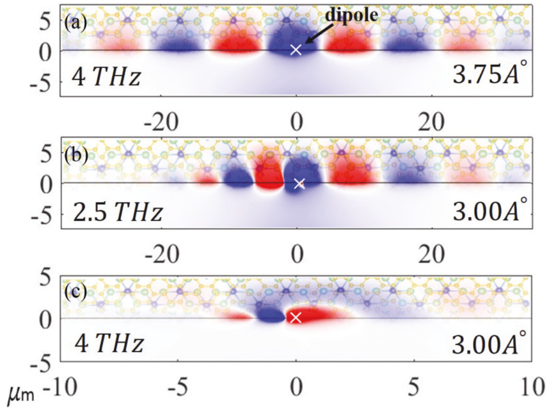

FIG. 8. Edge SPP launched by a dipole source near the graphene-vacuum edge for the exchange field magnetic bias corresponding to two CrI$_3$-graphene separations.

In contrast to Fig. 8, Fig. 9 shows the edge SPP on externally biased graphene due to a dipole source in the vicinity of the edge, computed using COMSOL. The size of the discontinuity is on the order of λ_{SPP} (e.g., the length of the discontinuity contour in the second panel is $5\lambda_{\mathrm{SPP}}$). It is clear that as the magnetic bias increases, the SPP propagates further, in agreement with Fig. 7, while its wavelength increases. The edge SPP is clearly robust, and propagates around the discontinuity. Although there appears to be a weak field to the left of the source, it is due to the imperfect boundary condition at the edge of the computational domain. (Converting to the time domain shows that the field to the left of the source is actually traveling towards the right.)

IV. FARADAY ROTATION

Faraday rotation on magnetically biased graphene has been studied in [19,44], among other works. As discussed above,

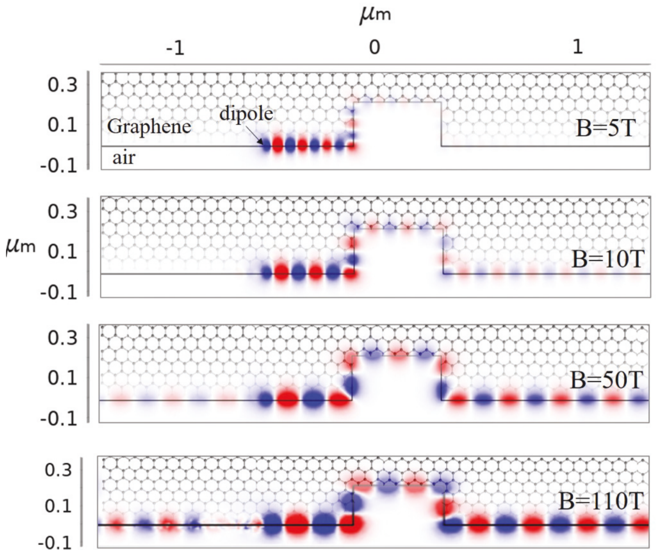

FIG. 9. Edge SPP launched by a dipole source near the graphene edge for several values of external magnetic bias. $f = 13.87$ THz, $\mu = 0.05$ eV, $T = 40$ K, $\Gamma = 2 \times 10^{12}$ s^{-1}.

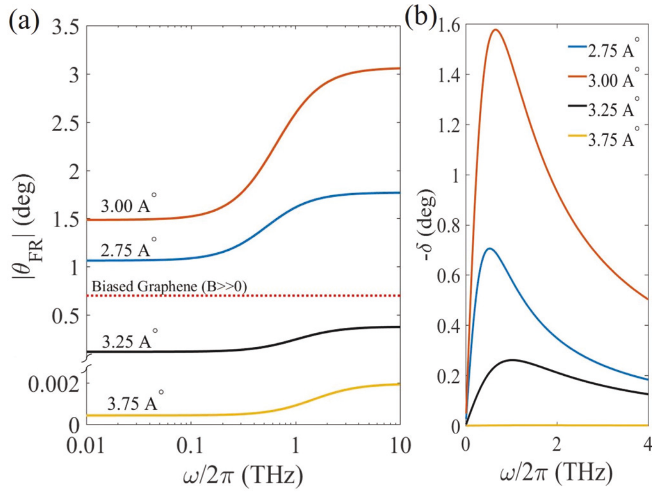

FIG. 10. (a) Faraday rotation and (b) ellipticity of the CrI_3-graphene heterostructure as a function of frequency for different separations. The dotted curve shows FR for externally-biased graphene using the effective field strengths from Fig. 3.

since the conductivity of the CrI_3 is much smaller than the conductivity of graphene at the considered frequencies, we can neglect the Faraday rotation contribution of the CrI_3, and only consider the FR of graphene under the influence of the exchange field. The Faraday rotation is computed as [45]

$$\theta_{FR} = \frac{1}{2}\arg\left(\frac{t_{pp} - it_{ps}}{t_{pp} + it_{ps}}\right), \tag{7}$$

and the ellipticity as

$$\delta = \frac{|t_{pp} - it_{ps}|^2 - |t_{pp} + it_{ps}|^2}{|t_{pp} - it_{ps}|^2 + |t_{pp} + it_{ps}|^2}, \tag{8}$$

where $t_{pp} = E_p^t/E_p^i,\ t_{ps} = E_s^t/E_p^i;\ p = x, y,\ s = x, y,\ s \neq p$; and the superscripts indicate incident (i) or transmitted (t) fields. For graphene in a homogeneous medium, the transmission coefficients are

$$t_{xx} = \frac{4/\eta + 2\sigma_{xx}}{4\sigma_{xx} + \eta(\sigma_{xx}^2 + \sigma_{xy}^2) + 4/\eta}, \tag{9}$$

$$t_{xy} = \frac{2\sigma_{xy}}{4\sigma_{xx} + \eta(\sigma_{xx}^2 + \sigma_{xy}^2) + 4/\eta}, \tag{10}$$

where $\eta = \sqrt{\mu/\varepsilon}$.

Faraday rotations for the exchange field case are shown in Fig. 10 for various CrI_3-graphene separations. For closer-than-equilibrium separations, modest Faraday rotations are observed, but for the equilibrium separation, FR is negligible since σ_{xy}/σ_{xx} is small. In contrast, for externally biased graphene, Fig. 11, large Faraday rotations can be obtained. As B increases, the FR resonance first blueshifts [Fig. 11(a)], and eventually stabilizes in frequency [Fig. 11(b)] at the first LL, but the peak FR continues to increase with increasing B. Ellipticity behaves in a similar manner as FR.

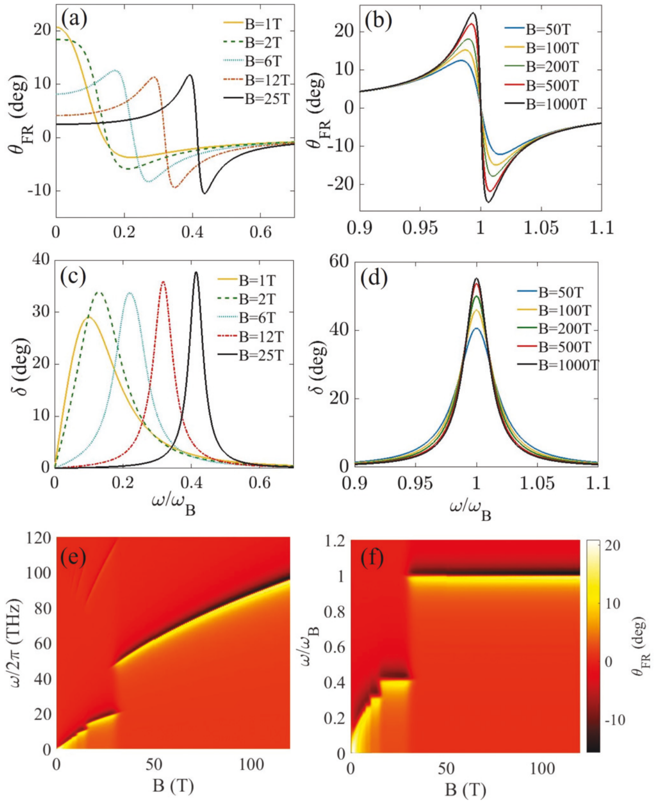

FIG. 11. (a),(b) Faraday rotation and (c),(d) ellipticity of graphene as a function of frequency for different external bias values, and (e),(f) density plots of Faraday rotation. ω_B is the frequency of the first Landau level for each bias. $\mu = 0.2\,\mathrm{eV}$, $T = 40\,\mathrm{K}$, and $\Gamma = 2\,\mathrm{THz}$.

V. CONCLUSIONS

We have examined exchange splitting in a monolayer chromium triiodide (CrI_3)–graphene vdW heterostructure using density-functional theory where effective exchange fields of hundreds of Tesla are predicted. These enormous fields serve as the magnetic bias for the graphene layer. Graphene conductivity and SPP properties for the exchange field were considered, and compared with the external bias case. Since no LLs occur for the exchange field, the resulting nonreciprocity is found to be considerably weaker than for an equivalent external field bias (where strongly nonreciprocal electromagnetic edge modes that are tightly confined, robust, and unidirectional are shown to exist). Faraday rotation due to the exchange field was also shown to be modest compared to the external bias case.

ACKNOWLEDGMENT

Funding for this research was provided by the National Science Foundation under Grant No. EFMA-1741673.

---

[1] K. S. Novoselov, A. K. Geim, S. V. Morozov, D. Jiang, Y. Zhang, S. V. Dubonos, I. V. Grigorieva, and A. A. Firsov, Electric field effect in atomically thin carbon films, Science. **306**, 666 (2004).

[2] S. D. Sarma, S. Adam, E. H. Hwang, and E. Rossi, Electronic transport in two-dimensional graphene, Rev. Mod. Phys. **83**, 407 (2011).

[3] M. A. McGuire, H. Dixit, V. R. Cooper, and B. C. Sales, Coupling of crystal structure and magnetism in the layered, ferromagnetic insulator $\mathrm{CrI_3}$, Chem. Mater. **27**, 612 (2015).

[4] B. Huang, G. Clark, E. Navarro-Moratalla, D. R. Klein, R. Cheng, K. L. Seyler, D. Zhong, E. Schmidgall, M. A. McGuire, D. H. Cobden, W. Yao, D. Xiao, P. Jarillo-Herrero, and X. D. Xu, Layer-dependent ferromagnetism in a van der Waals crystal down to the monolayer limit, Nature (London) **546**, 270 (2017).

[5] J. Liu, Q. Sun, Y. Kawazoe, and P. Jena, Exfoliating biocompatible ferromagnetic Cr-trihalide monolayers, Phys. Chem. Chem. Phys. **18**, 8777 (2016).

[6] W.-B. Zhang, Q. Qu, P. Zhu, and C.-H. Lam, Robust intrinsic ferromagnetism and half semiconductivity in stable two-dimensional single-layer chromium trihalides, J. Mater. Chem. C **3**, 12457 (2015).

[7] B. Huang, G. Clark, D. R. Klein, D. MacNeill, E. Navarro-Moratalla, K. L. Seyler, N. Wilson, M. A. McGuire, D. H. Cobden, D. Xiao, W. Yao, P. Jarillo-Herrero, and X. Xu, Electrical control of 2D magnetism in bilayer $\mathrm{CrI_3}$, Nat. Nanotech. **13**, 544 (2018).

[8] S. Jiang, L. Li, Z. Wang, K. F. Mak, and J. Shan, Controlling magnetism in 2D $\mathrm{CrI_3}$ by electrostatic doping, Nat. Nanotech. **13**, 549 (2018).

[9] D. J. O'Hara, T. Zhu, A. H. Trout, A. S. Ahmed, Y. K. Luo, C. H. Lee, M. R. Brenner, S. Rajan, J. A. Gupta, D. W. McComb, and R. K. Kawakami, Room temperature intrinsic ferromagnetism in epitaxial manganese selenide films in the monolayer limit, Nano Lett. **18**, 3125 (2018).

[10] M. Kan, S. Adhikari, and Q. Sun, Ferromagnetism in $\mathrm{Mn}X_2$ (X = S, Se) monolayers, Phys. Chem. Chem. Phys. **16**, 4990 (2014).

[11] X. Li and J. Yang, $\mathrm{CrXTe_3}$ (X = Si, Ge) nanosheets: two-dimensional intrinsic ferromagnetic semiconductors, J. Mater. Chem. C **2**, 7071 (2014).

[12] C. Gong, L. Li, Z. Li, H. Ji, A. Stern, Y. Xia, T. Cao, W. Bao, C. Wang, Y. Wang, Z. Q. Qiu, R. J. Cava, S. G. Louie, J. Xia, and X. Zhang, Discovery of intrinsic ferromagnetism in two-dimensional van der Waals crystals, Nature (London) **546**, 265 (2017).

[13] K. Zollner, P. E. Faria Junior, and J. Fabian, Proximity exchange effects in $\mathrm{MoSe_2}$ and $\mathrm{WSe_2}$ heterostructures with $\mathrm{CrI_3}$: Twist angle, layer, and gate dependence, Phys. Rev. B **100**, 085128 (2019).

[14] J. Zhang, B. Zhao, T. Zhou, Y. Xue, C. Ma, and Z. Yang, Strong magnetization and Chern insulators in compressed graphene/$\mathrm{CrI_3}$ van der Waals heterostructures, Phys. Rev. B **97**, 085401 (2018).

[15] N. Levy, S. A. Burke, K. L. Meaker, M. Panlasigui, A. Zettl, F. Guinea, A. H. Castro Neto, M. F. Crommie, Strain-induced pseudo–magnetic fields greater than 300 tesla in graphene nanobubbles, Science **329**, 544 (2010).

[16] J. Zhang, B. Zhao, Y. Yao, and Z. Yang, Robust quantum anomalous Hall effect in graphene-based van der Waals heterostructures, Phys. Rev. B **92**, 165418 (2015).

[17] P. Wei, S. Lee, F. Lemaitre, L. Pinel, D. Cutaia, W. Cha, F. Katmis, Y. Zhu, D. Heiman, J. Hone, J. S. Moodera, and C.-T. Chen, Strong interfacial exchange field in the graphene/EuS heterostructure, Nat. Mater. **15**, 711 (2016).

[18] Z. H. Qiao, S. A. Yang, W. X. Feng, W. K. Tse, J. Ding, Y. G. Yao, J. Wang, and Q. Niu, Quantum anomalous Hall effect in graphene from Rashba and exchange effects, Phys. Rev. B **82**, 161414(R) (2010).

[19] I. Fialkovsky and D. V. Vassilevich, Faraday rotation in graphene, Eur. Phys. J. B **85**, 384 (2012).

[20] T. M. Slipchenko, J. Schiefele, F. Guinea, and L. Martin-Moreno, Strain-induced large Faraday rotation in graphene at subtesla external magnetic fields, Phys. Rev. Research **1**, 033049 (2019).

[21] C. Cardoso, D. Soriano, N. A. García-Martínez, and J. Fernández-Rossier, Van der Waals Spin Valves, Phys. Rev. Lett. **121**, 067701 (2018).

[22] Y. V. Bludov, J. N. Gomes, G. A. Farias, J. Fernández-Rossier, M. I. Vasilevskiy, and N. M. R. Peres, Hybrid plasmon-magnon polaritons in graphene-antiferromagnet heterostructures, 2D Mater. **6**, 045003 (2019).

[23] See Supplemental Material at http://link.aps.org/supplemental/10.1103/PhysRevB.102.075435 for additional discussion of the DFT calculations and the derivation of the edge plasmon dispersion, which includes Refs. [24–28].

[24] M. Gajdoš, K. Hummer, G. Kresse, J. Furthmüller, and F. Bechstedt, Linear optical properties in the projector-augmented wave methodology, Phys. Rev. B **73**, 045112 (2006).

[25] A. L. Fetter, Edge magnetoplasmons in a bounded two-dimensional electron fluid, Phys. Rev. B **32**, 7676 (1985).

[26] W. Wang, J. Kinaret, and P. Apell, Excitation of edge magnetoplasmons in semi-infinite graphene sheets: Temperature effects, Phys. Rev. B **85**, 235444 (2012).

[27] G. W. Hanson and A. B. Yakovlev, *Operator Theory for Electromagnetics: An Introduction* (Springer, New York, 2002).

[28] X. Xia and J. J. Quinn, Multipole edge plasmons of two-dimensional electron-gas systems, Phys. Rev. B **50**, 8032 (1994).

[29] M. Wu, Z. Li, T. Cao, and Steven G. Louie, Physical origin of giant excitonic and magneto-optical responses in two-dimensional ferromagnetic insulators, Nat. Commun. **10**, 2371 (2019).

[30] G. Kresse and J. Furthmüller, Efficient iterative schemes for ab initio total-energy calculations using a plane-wave basis set, Phys. Rev. B **54**, 11169 (1996).

[31] S. L. Dudarev, G. A. Botton, S. Y. Savrasov, C. J. Humphreys, and A. P. Sutton, Electron-energy-loss spectra and the structural stability of nickel oxide: An LSDA+U study, Phys. Rev. B **57**, 1505 (1998).

[32] S. Grimme, J. Antony, S. Ehrlich, and S. Krieg, A consistent and accurate *ab initio* parametrization of density functional dispersion correction (DFT-D) for the 94 elements H-Pu, J. Chem. Phys. **132**, 154104 (2010); S. Grimme, S. Ehrlich, and L. Goerigk, J. Comput. Chem. **32**, 1456 (2011).

[33] J. W. Davenport, R. E. Watson, and M. Weinert, Linear augmented-Slater-type-orbital method for electronic-structure calculations. V. Spin-orbit splitting in $\mathrm{Cu_3Au}$, Phys. Rev. B **37**, 9985 (1988); Y. Qi, S. H. Rhim, G. F. Sun, M. Weinert, and L. Li, Phys. Rev. Lett. **105**, 085502 (2010).

[34] M. X. Chen and M. Weinert, Layer k-projection and unfolding electronic bands at interfaces, Phys. Rev. B **98**, 245421 (2018).

[35] P. Nigge, A. C. Qu, É. Lantagne-Hurtubise, E. Mårsell, S. Link, G. Tom, M. Zonno, M. Michiardi, M. Schneider, S. Zhdanovich, G. Levy, U. Starke, C. Gutiérrez, D. Bonn, S. A. Burke, M. Franz, and A. Damascelli, Room temperature strain-induced Landau levels in graphene on a wafer-scale platform, Science Adv. **5**, eaaw5593 (2019).

[36] V. P. Gusynin, S. G. Sharapov, and J. P. Carbotte, Magneto-optical conductivity in graphene, J. Phys.: Condens. Matter **19**, 026222 (2007).

[37] G. W. Hanson, Quasi-TEM Modes Supported by a Graphene Parallel-Plate Waveguide, J. Appl. Phys. **104**, 084314 (2008).

[38] G. W. Hanson, Dyadic Green's Functions for an Anisotropic, Non-Local Model of Biased Graphene, IEEE Trans. Ant. Propagat. **56**, 747 (2008).

[39] A. Ishimaru, *Electromagnetic Wave Propagation, Radiation, and Scattering* (Prentice Hall, Upper Saddle River, NJ, 1991).

[40] R. Camley, Nonreciprocal surface waves, Surf. Sci. Rep. **7**, 103 (1987).

[41] D. B. Mast, A. J. Dahm, and A. L. Fetter, Observation of Bulk and Edge Magnetoplasmons in a Two-Dimensional Electron Fluid, Phys. Rev. Lett. **54**, 1706 (1985).

[42] Weihua Wang, Peter Apell, and Jari Kinaret, Edge plasmons in graphene nanostructures, Phys. Rev. B **84**, 085423 (2011).

[43] In the $B = 0$ case, the SPP is not formed for $\hbar\omega \gg \mu$ (states are not filled). In the external magnetic bias case, the value of B plays a role, with larger B moving the first LL to higher frequencies, increasing the band gap.

[44] I. Crassee, J. Levallois, A. L. Walter, M. Ostler, A. Bostwick, E. Rotenberg, T. Seyller, D. van der Marel, and A. B. Kuzmenko, Giant Faraday rotation in single- and multilayer graphene, Nat. Phys. **7**, 48 (2011).

[45] A. Ferreira, J. Viana-Gomes, Yu. V. Bludov, V. Pereira, N. M. R. Peres, and A. H. Castro Neto, Faraday effect in graphene enclosed in an optical cavity and the equation of motion method for the study of magneto-optical transport in solids, Phys. Rev. B **84**, 235410 (2011).